

## LES study of turbulence intensity impact on spark ignition in a two-phase flow

J. STEMPKA, L. KUBAN, A. TYLISZCZAK

*Faculty of Mechanical Engineering and Computer Science  
Institute of Thermal Machinery  
Czestochowa University of Technology  
Armii Krajowej 21  
42-201 Czestochowa, Poland  
e-mail: stempka@imc.pcz.pl*

THE PAPER PRESENTS LARGE EDDY SIMULATION (LES) study aiming at investigations of an influence of flow conditions on a spark ignition process in a two-phase shear dominated flow. Implicit LES approach is applied for the combustion modelling and the spark is modelled using the energy deposition model of LACAZE *et al.* [20]. We examine an impact of turbulence intensities and randomness of initial distributions of velocity fluctuations on a flame development during the spark duration and shortly after it is switched off. It is found that for a strong spark, as used in IC engines, the turbulence intensity has little effect on the ignition and flame kernel growth and no significant differences are seen even if the turbulence intensities differ four times. It is observed that weak turbulent structures cannot affect fast flame propagation mechanism and its development is conditioned by evaporation and rapid thermal expansion. In such regimes, the turbulence seems to be too weak to significantly alter the flame dynamics. It is found that at the initial stage of the flame development it grows toward the fuel-rich region and spread over the fuel-lean side only after the evaporated fuel diffuses and mixes with the oxidizer stream. The flame size and its shape turn out to be equally dependent on the initial distribution of the turbulence fluctuations and turbulence intensity.

**Key words:** LES, spray combustion, spark ignition, mixing layer.

Copyright © 2018 by IPPT PAN

### 1. Introduction

LIQUID FUELS ARE COMMONLY USED IN ALL TYPES OF ENGINES (cars, planes, ships) and industrial devices (burners, combustion chambers, etc.) and constitute a field of extensive research both in academia and in industry. The process of spark ignition analysed in this work is of a critical importance for, e.g., aeronautics where the efficient and reliable ignition (or altitude re-ignition) is required for engines certification. Analysis of the ignition is very complicated from both the theoretical and experimental point of view. It is influenced

by a range of interlinked phenomena: (i) droplet dispersion and evaporation; (ii) mixing of fuel vapour; (iii) and finally chemical reactions being induced by a spark.

The complexity of ignition causes that its modelling must have a multidisciplinary character, combining physics of flows, phase change phenomena and chemical reactions [1, 2]. Numerical modelling of the spark ignition generated either from the electrodes or from the laser pulse is hardly possible and simplified models are used. It is a relatively new topic and is subjected to very extensive research both numerical [3–6] and experimental [7, 8]. Large eddy simulations (LES) studies [9–11] are usually done in simplified domains focusing on demonstration that modelling the spark ignition may be treated as a useful predictive tool. Research performed with the help of direct numerical simulations (DNS) concern mainly the theoretical issues and are carried out always for fundamental configurations, e.g. for a decaying turbulence [12, 13]. The study of the spark ignition in inhomogeneous methane-air mixtures [14] was performed by DNS simulation in the turbulent flow fields of different turbulence intensities. Extensive numerical research on forced ignition in monodisperse spray was done by NEOPHYTOU *et al.* [15] in which the 3D DNS simulations of two-phase flows with complex chemistry for n-heptane were conducted. The DNS simulation of forced ignition in a turbulent mixing layer was performed in [16] in order to investigate the effects of mixture fraction and its gradient. More recent numerical research, treating the non-premixed spark ignition and combustion have been performed for jets [17], counterflows [18] and bluff bodies [19]. The common observations, which can be formulated based on the aforementioned papers are as follow: (i) the success or failure of spark ignition strongly depends on location of the spark and conditions of the flow around it; (ii) small and short-lasting sparks (i.e. with low energy content) fail to ignite and generally sprays ignite later than similar premixed gaseous mixtures; (iii) rapid evaporation facilitates ignition; (iv) increased turbulence intensity may have both negative or positive effect on ignition.

In general, in contrary to gaseous flows where the ignition mechanisms are relatively well recognized, the knowledge of ignition in liquid fuelled systems is much less advanced. This is because of increased multidisciplinary of research in such systems, which besides of strongly unsteady physicochemical interactions (flow-flame) have to deal with the interfacial interactions (e.g. atomisation, coalescence, droplets-gas coupling) and phase change phenomenon. The present work is dedicated to investigate the influence of the flow parameters detrimental to flame initiation and propagation. We focus on a turbulent reacting droplet-laden flow in which an imposed initial turbulent velocity field causes the spatio-temporal development of the shear layer. The analysed cases are selected in order to reflect the importance of global and local flow parameters.

## 2. Model description

In this work we consider the low Mach number, reacting two-phase flow for which the LES approximated Navier–Stokes equations complemented with the equation of state are given as:

$$(2.1) \quad \frac{\partial \bar{\rho}}{\partial t} + \frac{\partial \bar{\rho} \tilde{u}_j}{\partial x_j} = \bar{S}_{mass},$$

$$(2.2) \quad \frac{\partial \bar{\rho} \tilde{u}_i}{\partial t} + \frac{\partial \bar{\rho} \tilde{u}_i \tilde{u}_j}{\partial x_j} = -\frac{\partial \bar{p}}{\partial x_i} + \frac{\partial \bar{\tau}_{ij}}{\partial x_j} + \frac{\partial \tau_{ij}^{sgs}}{\partial x_j} + \bar{S}_{m,i},$$

$$(2.3) \quad p_0 = \bar{\rho} R \tilde{T},$$

where the bars and tildes denote the LES filtered and Favre averaged quantities. The symbols  $p_0$  and  $R$  are thermodynamic pressure and gas constant, respectively. The variables:  $u, \rho, p, T$  denote the velocity component, density, hydrodynamic pressure and temperature. The terms  $\tau_{ij}$  and  $\tau_{ij}^{sgs}$  represent the viscous and the sub-grid stress tensors. The latter is related to the strain rate tensor  $\tilde{S}_{ij}$  by the expression  $\tau_{ij}^{sgs} = 2\mu_{sgs}\tilde{S}_{ij}$ , where the sub-grid viscosity  $\mu_{sgs}$  is calculated using the Vreman model [20]. The source terms  $\bar{S}_{mass}$  and  $\bar{S}_{m,i}$  originate from the two-way coupling between the droplets and the gas phase and their definitions are discussed in Subsection 2.1.1. The species ( $\phi_\alpha$ ) and the enthalpy ( $h$ ) transport equations are given by:

$$(2.4) \quad \frac{\partial \bar{\rho} \tilde{\phi}_\alpha}{\partial t} + \frac{\partial \bar{\rho} \tilde{\phi}_\alpha \tilde{u}_j}{\partial x_j} = \frac{\partial}{\partial x_j} \left[ \left( \frac{\mu}{\sigma} + \frac{\mu_{sgs}}{\sigma_{sgs}} \right) \frac{\partial \tilde{\phi}_\alpha}{\partial x_j} \right] + \bar{S}_\alpha + \bar{\rho} \tilde{\dot{\omega}}(\phi_\alpha),$$

$$(2.5) \quad \frac{\partial \bar{\rho} \tilde{h}}{\partial t} + \frac{\partial \bar{\rho} \tilde{h} \tilde{u}_j}{\partial x_j} = \frac{\partial}{\partial x_j} \left[ \left( \frac{\mu}{\sigma} + \frac{\mu_{sgs}}{\sigma_{sgs}} \right) \frac{\partial \tilde{h}}{\partial x_j} \right] + \bar{S}_h + \dot{Q},$$

where the subscript  $\alpha$  denotes the species index from 1 to N-species. The symbols  $\sigma$  and  $\sigma_{sgs}$  refer to the Prandtl/Schmidt numbers and their turbulent counterpart. They are assumed equal to 0.7 and 0.9, respectively. The source terms  $\bar{S}_\alpha$  and  $\bar{S}_h$  are responsible for production of the fuel vapour and the energy exchange between the gas phase and droplets (see Section 2.1.1). The liquid phase is modelled in the Lagrangian reference frame (Subsection 2.1.2) with the two-way coupling. The droplets are presumed to act as point sources of mass, momentum and energy. They modify the gaseous phase depending on the relative velocity (droplets/gas phase), temperature and the fuel mass fraction. The source term  $\dot{Q}$  represents the energy flux deposited from the spark, it is discussed in Subsection 2.1.3. The species reaction rates  $\tilde{\dot{\omega}}(\phi_\alpha)$  are computed using Implicit LES technique (ILES) discussed in Subsection 2.1.4.

### 2.1. Source terms

**2.1.1. Phase coupling.** Applying the two-way coupling, the gas phase acts on the droplets and the droplets act on the gas phase through the source terms appearing in Eqs. (2.1) to (2.5). They represent averaged sums of the contributions from all ( $N_p$ ) particles at each computational cell, i.e., generally one may write  $\bar{S} = 1/V \sum_{p=1}^{N_p} \dot{S}_p$  where  $V$  and  $p$  denote the cell volume and  $p$ -th droplet, respectively. The expressions of source terms are formulated as:

$$(2.6) \quad \bar{S}_{mass,p} = \bar{S}_{\alpha,p} = -\frac{d}{dt}(m_d)_p,$$

$$(2.7) \quad \bar{S}_{m,p} = -\frac{d}{dt}(m_d v_d)_p,$$

$$(2.8) \quad \bar{S}_{h,p} = -\frac{d}{dt}(m_d c_L T_d)_p,$$

where  $m_d$ ,  $v_d$ ,  $T_d$  are the droplet's mass, velocity and temperature, respectively. Symbol  $c_L$  denotes the specific heat capacity of the liquid fuel.

**2.1.2. Droplets motion and evaporation.** The dispersed phase motion and evaporation is analysed in the Lagrangian reference frame, following the model of MILLER *et al.* [21], where the position and velocity of the droplets are computed from:

$$(2.9) \quad \frac{d\mathbf{x}_d}{dt} = \mathbf{v}_d,$$

$$(2.10) \quad \frac{d\mathbf{v}_d}{dt} = \frac{\tilde{\mathbf{u}} - \mathbf{v}_d}{\tau_d^v},$$

where  $\tilde{\mathbf{u}}$  is the gas phase velocity at the droplet's position and  $\tau_d^v$  is the relaxation time defined as:

$$(2.11) \quad \frac{1}{\tau_d^v} = \frac{3}{8} \frac{\rho_L}{\rho} \frac{C_D}{r_d} |\tilde{\mathbf{u}} - \mathbf{v}_d|,$$

where  $\rho_L$  is the liquid fuel density,  $C_D$  denotes drag coefficient and  $r_d$  is the droplet radius.

The evaporation process is described by the following set of equations representing the droplet temperature and mass changes:

$$(2.12) \quad \frac{dT}{dt} = \frac{\text{Nu}}{3\text{Pr}} \left( \frac{1}{\tau_d} \frac{C_{P,g}}{c_L} \right) (\tilde{T} - T_d) + \left( \frac{L_v}{c_L} \right) \frac{\dot{m}_d}{m_d},$$

$$(2.13) \quad \frac{dm_d}{dt} = -\frac{\text{Sh}}{3\text{Sc}} \left( \frac{m_d}{\tau_d} \right) \ln(1 + B_M).$$

The Nusselt and Sherwood numbers (Nu and Sh) include convective and blowing effects and are computed as in [21]. The symbol  $\tilde{T}$  denotes the gas temperature at the droplet's position and  $L_v$  is the latent heat of evaporation. The symbols Sc and Pr are the Schmidt and Prandtl numbers,  $C_{P,g}$  is the fuel vapour heat capacity and  $B_M$  denotes the Spalding mass transfer number. The particle relaxation time is defined as  $\tau_d = \rho_L D^2 / 18\mu$  in which  $D$  is the droplet's diameter and  $\mu$  is the fuel vapour dynamic viscosity.

**2.1.3. Spark.** We use a simplified model of the spark (energy deposition model [22]) in which the spark has purely thermal effect, described by the local increase of the energy (or temperature). In this approach the source term  $\dot{Q}$  is added to the enthalpy equation. The spark's energy flux follows the Gaussian distribution in time and space and is defined as:

$$(2.14) \quad \dot{Q} = \frac{\epsilon}{4\pi^2 \sigma_s^3 \sigma_t} \exp\left[-\frac{1}{2} \left(\frac{r}{\sigma_s}\right)^2\right] \exp\left[-\frac{1}{2} \left(\frac{t-t_0}{\sigma_t}\right)^2\right],$$

where  $r$  is the radial distance to the center of the spark,  $t$  denotes time and  $t_0$  is the time when  $\dot{Q}$  reaches a maximum. The spark source term is controlled by the total amount of energy deposited  $\epsilon$  and two model parameters  $\sigma_s = \Delta_s/a$  and  $\sigma_t = \Delta_t/a$  where  $\Delta_s$  and  $\Delta_t$  are the characteristic size and time duration of the spark, respectively. The coefficient  $a = 4\sqrt{\ln(10)}$  is chosen so that 98% of the energy deposited finds in the domain  $\Delta_s^3 \cdot \Delta_t$ .

**2.1.4. Reaction rate.** The reaction rates  $\overline{\dot{\omega}}(\phi_\alpha)$  are obtained from the Arrhenius formulas and are computed using ILES approach [23] based on the filtered flow variables as  $\overline{\dot{\omega}_\alpha(Y, h)} \approx \dot{\omega}_\alpha(\tilde{Y}, \tilde{h})$ . The ILES assumption would certainly fail in the Reynolds Averaged Navier–Stokes (RANS) framework as the fluctuations in RANS models are large in general. On the other hand, the ILES is valid for the laminar flow simulation and in DNS where all turbulent flow scales are resolved. Hence, one may assume that for sufficiently dense computational meshes, when the grid cells are comparable with the Kolmogorov length scale (as it takes place in the present work), the ILES approach is appropriate. Note that the sub-filter scales resulting from the filtration of the convective terms are modelled as usually with the eddy viscosity model applied. Similarly, as in many previous works, e.g. [12, 14, 16] we assume a global one-step chemical reaction  $\text{C}_2\text{H}_5\text{OH} + 3(\text{O}_2 + 3.76\text{N}_2) = 2\text{CO}_2 + 3(\text{H}_2\text{O} + 3.76\text{N}_2)$ . Such an approach minimizes the computational expense but is known from over-predicting the flame speed in the rich mixtures, as discussed in [16]. To correct this weakness and to give reasonable predictions of the strain rate extinction the reaction rates are tuned as in [24].

## 2.2. Numerical approach

Simulations are carried out using an in-house academic LES solver based on the high-order compact difference method combined with the projection method for pressure-velocity coupling on half-staggered meshes and the  $2^{nd}$  order TVD scheme for convective term discretisation in the species transport equations [25, 26]. The time integration scheme is based on the predictor-corrector approach with the combinations of Adams–Bashforth and Adams–Moulton methods. The equations for the droplets velocity, position, mass and temperature are integrated in time with the Euler explicit method. The flow variables are interpolated at the droplets positions using the  $4^{th}$  order Lagrangian interpolation polynomial and the sources of the momentum, mass and energy originating from the droplets are redistributed to the grid points with the help of the  $2^{nd}$  order trilinear interpolation. The code was thoroughly verified and used in previous studies [27–30].

## 2.3. Computational configuration

Figure 1 shows the computational domain used in the studies. It comprises a rectangular box with the following dimensions  $L_x = 0.025$  m,  $L_y = 0.04$  m and  $L_z = 0.01$  m. The periodic boundary conditions are defined in the  $x$  and  $z$  directions and isothermal moving walls at  $y = \pm L_y/2$ . Initially, two streams of

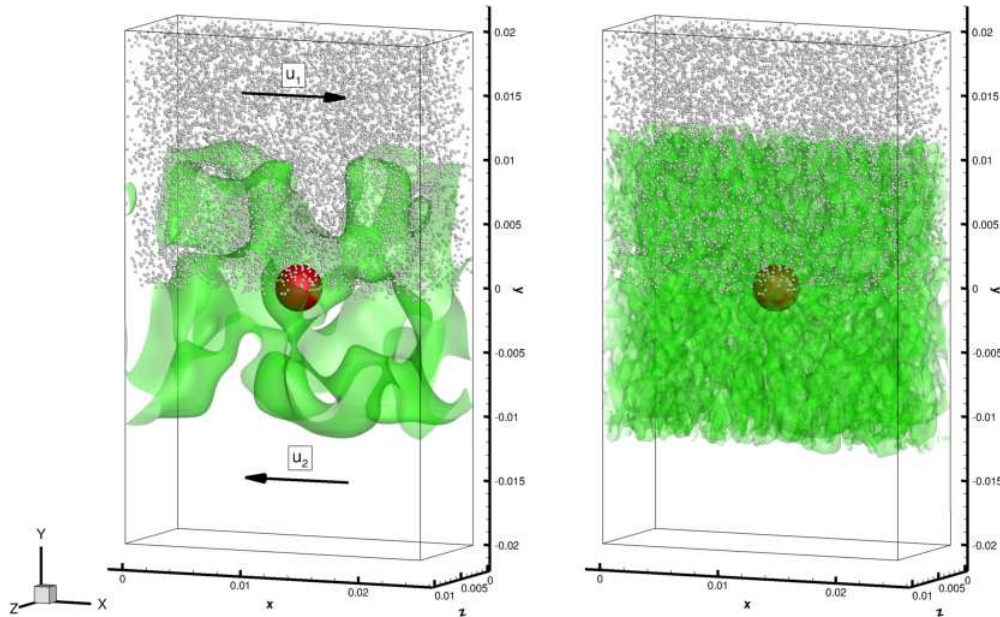


FIG. 1. Representation of the computational domain showing initial droplet distribution, spark location and isosurface of the arbitrary chosen horizontal velocity component value. Different scales sizes are showed for cases:  $Ti = 1\%$  (left) and  $Ti = 4\%$  (right).

air at atmospheric conditions (101325 Pa, 300 K) flow in the opposite directions. The velocity profile between the upper and lower stream is defined by the hyperbolic tangent function  $u(y) = U_\infty \tanh(2y/\delta)$  in which the free stream velocity  $U_\infty$  is computed based on the specified Reynolds number  $Re_\delta = U_\infty \delta / \nu = 50$ . The vorticity thickness is given as  $\delta = 2U_\infty / |du/dy|_{\max} = 1 \cdot 10^{-3}$  m and the air kinematic viscosity  $\nu$  value is taken based on the initial conditions. The velocity field in the region of the mixing layer ( $\pm 20\delta$ ) is initially disturbed by the superimposed isotropic turbulence field. It is computed from the Passot–Pouquet kinetic energy spectrum defined as [31]:

$$(2.15) \quad E(k, y) = 16\sqrt{2/\pi} \frac{u'^2}{k_0} \left(\frac{k}{k_0}\right)^4 \exp\left[-2\left(\frac{k}{k_0}\right)^2\right]$$

where  $k_0$  is an adjustable wave number used to generate the turbulence field with required Taylor length scale defined as  $\lambda = \langle \sqrt{u'u'} \rangle / \langle \partial(u'u') / \partial x \rangle$  where  $u'$  is the initial velocity fluctuations calculated as  $u' = T_i U_\infty$  with the specified turbulence intensity  $T_i$ . We consider two cases with significantly different turbulence intensities, i.e.,  $T_i = 1\%$  and  $T_i = 4\%$ . The Passot–Pouquet turbulence kinetic energy spectrum (TKE) is known to skip the inertial range, and hence, one can assume that initial conditions differ mainly at the small flow scales of the order of the Kolmogorov length scale  $\eta_K$ . The turbulence field generator requires random set of numbers, which are then used to generate a velocity field that follows specified TKE spectrum but differs in spatial distribution of the velocity fluctuations. To check the influence of the randomness of the velocity fluctuations on the results we use two different random number “seeds” to generate two distinct initial velocity fields (s1 and s2). Figure 1 illustrates the initial velocity fields showing the flows scales for two different turbulence intensities.

As the fuel, we considered the ethanol monodispersed spray with the droplets’ diameter equal to  $D = 100$   $\mu\text{m}$ . Initially, the droplets were randomly scattered in the upper part of the domain. Their initial temperature was equal to  $T_d = 300$  K and their velocities were the same as the local velocities of the gas phase at corresponding locations. The total fuel mass load was equal to  $4 \cdot 10^{-7}$  kg that resulted in the fuel to air volume fraction less than the threshold value  $10^{-4}$  distinguishing

**Table 1. Parameters of the simulated cases.  $Re_\lambda$  is the Reynolds number defined based on the Taylor length scale.**

Case	seed [-]	$T_i$ [%]	$u'$ [m/s]	$\eta_K$ [m]	$Re_\lambda$ [-]
s1Ti1	1	1	$0.8 \times 10^{-2}$	$1.2 \times 10^{-3}$	1.2
s2Ti1	2	1	$0.8 \times 10^{-2}$	$1.2 \times 10^{-3}$	1.2
s1Ti4	1	4	$3.2 \times 10^{-2}$	$0.6 \times 10^{-3}$	1.2
s2Ti4	2	4	$3.2 \times 10^{-2}$	$0.6 \times 10^{-3}$	1.2

a diluted regime. The parameters of four test cases are detailed in Table 1. They are referred to anywhere further in this work by symbol sXTiY, where X denotes the initial random disturbance and Y corresponds to the turbulence intensity. The mesh sizes in terms of the Kolmogorov length scale ( $\eta_K$ ) are equal to: (i) for  $Ti = 1\%$  the  $\eta_K = 1.2\delta$  while  $\Delta x = 0.08\eta_K$ ,  $\Delta y_{min} = 0.05\eta_K$  and  $\Delta z = 0.13\eta_K$ ; (ii) for  $Ti = 4\%$  the  $\eta_K = 0.6\delta$  while  $\Delta x = 0.16\eta_K$ ,  $\Delta y_{min} = 0.1\eta_K$  and  $\Delta z = 0.26\eta_K$ . In each case the spark was initiated at  $t = 4.75 \text{ ms}$ , it lasted for  $\Delta t = 0.5 \text{ ms}$  and the maximum value of  $\dot{Q}$  occurred at  $t_{sp} = 5 \text{ ms}$ . The size of the spark and its total energy were equal to  $\Delta_s = 3 \text{ mm}$  and  $\epsilon = 8 \text{ mJ}$ , respectively. The applied spark is relatively strong, its energy is much above the minimum ignition energy for ethanol/air mixtures and is in the range of ignition energies applied in IC engines.

### 3. Results

#### 3.1. General overview

In all cases, the spark was placed in the center of the domain at point  $0.0125 \text{ m}$ ,  $0.0 \text{ m}$ ,  $0.005 \text{ m}$  in  $x$ ,  $y$ ,  $z$  coordinates respectively. The analysis of the results is limited to the flame initiation and its early stage of development. Figures 2a) and b) show the progress of the flame kernel development shortly after the spark ignition in two different flow regimes (s1Ti1 and s1Ti4). It can be seen that both kernels are very little affected by the flow field. Such a behaviour

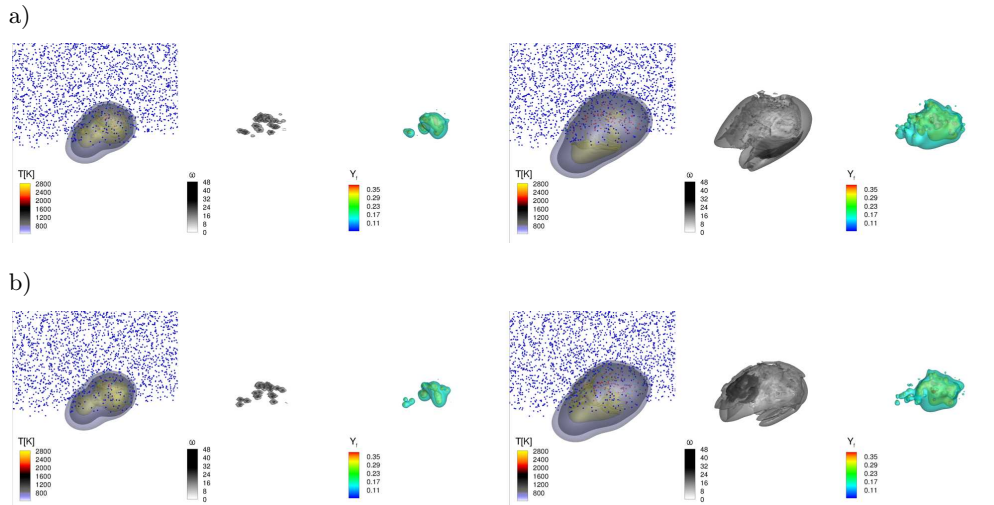


FIG. 2. Evolution of the flame kernel in two subsequent time instances ( $1.2t_{sp}$  and  $1.4t_{sp}$ ) represented by the isosurfaces of: temperatures (left), vorticity (center) and fuel mass fraction (right). Turbulence intensity: a)  $Ti = 1\%$ , b)  $Ti = 4\%$ .

at first sight may seem very surprising. However, if we consider that the velocity fluctuation level is generally low, of the order of  $10^{-2}$  m/s it becomes obvious that a relatively slow small-scale motion cannot affect a fast flame propagation mechanism. Hence, even if the turbulence intensity differs four times it has no significant influence on the flame kernel. In addition, its development is dominated by the mechanism of rapid thermal expansion and hence the turbulence seems to be too weak to wrinkle the flame. One may observe that the flame volume grows faster in the upper fuel-rich side towards which the flame propagates.

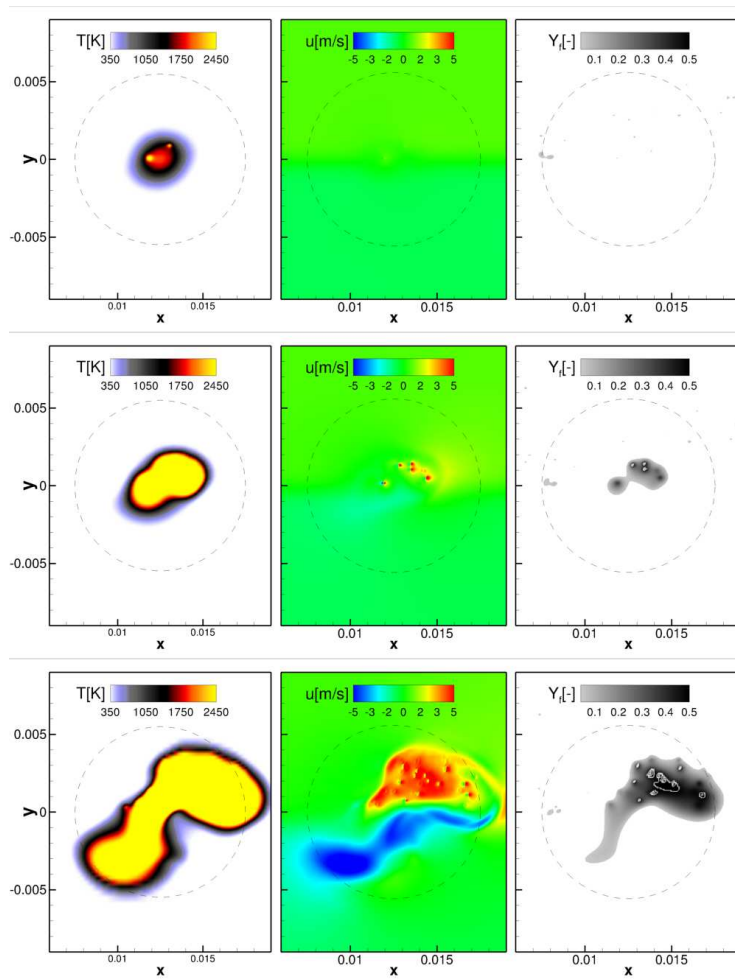


FIG. 3. Evolution of the high temperature region in three subsequent time instances ( $1.05t_{sp}$ ,  $1.2t_{sp}$  and  $1.4t_{sp}$ ) represented by the surface plots of: temperatures (left), u-velocity component (center) and fuel mass fraction (right) for low turbulence intensity  $Ti = 1\%$ . The dashed envelope indicates size and position of the spark.

Figures 3 and 4 show the temporal evolution of temperature, the magnitude of the horizontal velocity component and fuel mass fraction plotted on  $z$ -normal plane at  $z = 0.5$  for two cases s1Ti1 and s1Ti4, respectively. It is clear that initially high temperature region has been evolving symmetrically during energy deposition stage. During the flame development, this region becomes more asymmetrical as moving towards the rich-fuel side. In the former case, the high temperature region grows mainly by the gas expansion mechanism after the reaction was initiated. Its growth speed is determined by the heat diffusion rate. One can observe that due to the thermal expansion, the velocity component boosts outwardly with the direction of the flame velocity.

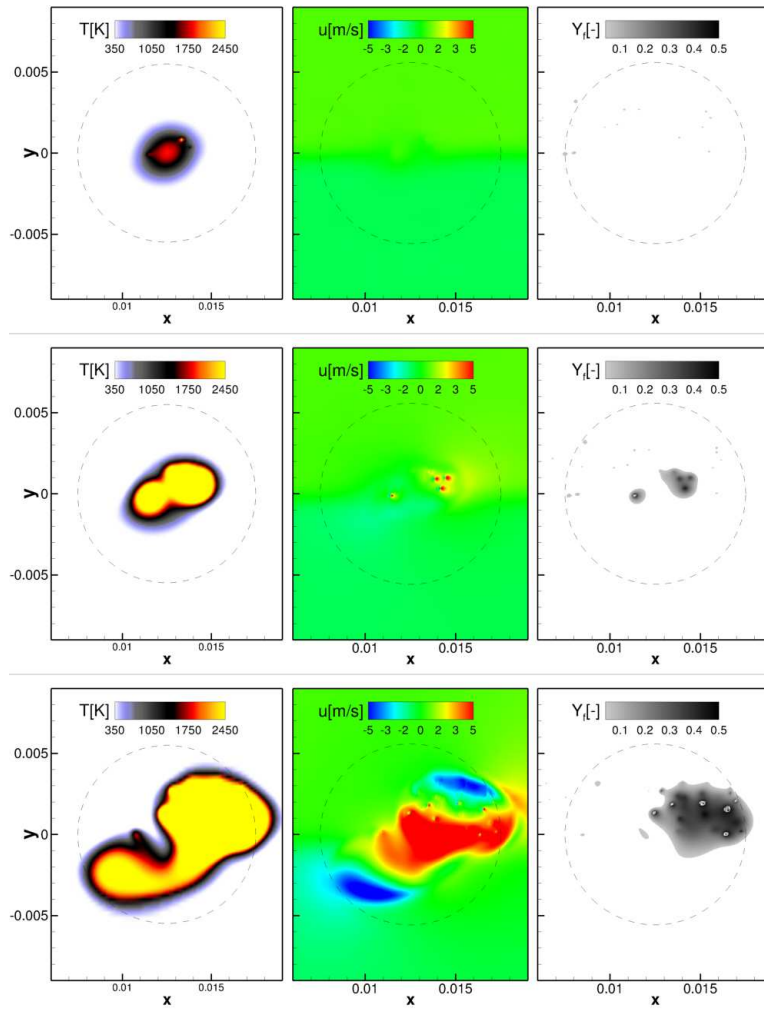


FIG. 4. As in Fig. 3 for turbulence intensity  $Ti = 4\%$ .

The ignition scenario presented in Fig. 4 for the case s1Ti4 is alike s1Ti1. Comparing the area of high temperature region one may assume that for both turbulent intensities the flame grows in a similar manner. This is also confirmed in Fig. 5 which shows temporal evolution of the maximum temperature and the flame volume ( $V = \sum V_{cells}$  in which  $T > 1200$  K). One may observe that even though the maximum temperature raised more quickly for lower turbulent intensities (cases s1Ti1 and s2Ti1), the instantaneous flame volume growth seems to depend more on the randomness of the initial velocity field. Indeed, for the cases s1T1 and s1T4 the flames are definitely larger. The evolution of maximum temperature (Fig. 5a) shows its constant level at 3000 K. This is the effect of the upper temperature limit artificially assumed in the code for stability reason.

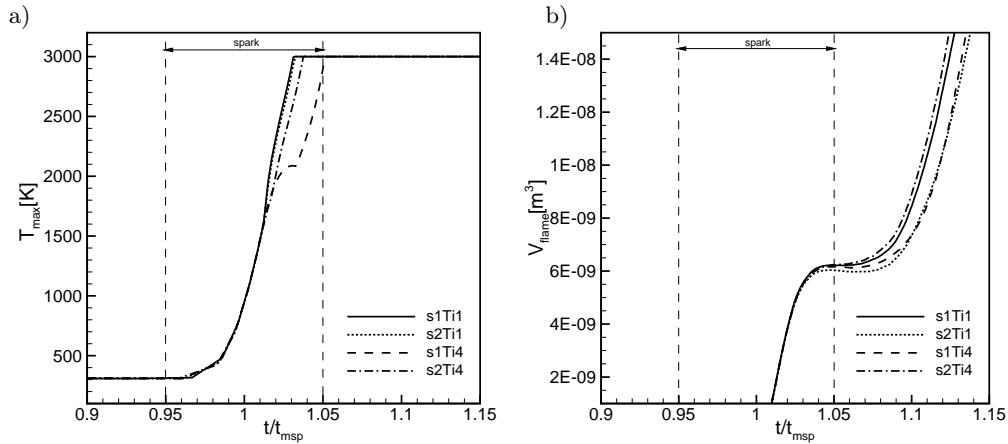


FIG. 5. Plots of the maximum temperature (a) and flame volume growth (b) in a function of the non-dimensional spark time.

Figure 6 shows the plots of mean values of a mixture fraction  $\xi$  as a function of normalized  $y$ -distance  $y_{norm} = y/L_y$  in two time instances  $1.2t_{sp}$  and  $1.4t_{sp}$ . The mixture fraction is defined as  $\xi = (\nu Y_f - Y_{O_2} + Y_{O_2,2})/(\nu Y_{f,1} + Y_{O_2,2})$  where  $\nu$  is the stoichiometric coefficient,  $Y_f$  and  $Y_{O_2}$  are the local fuel and oxygen mass fractions,  $Y_{f,1}$  and  $Y_{O_2,2}$  are the fuel and oxygen mass fractions in the fuel/oxidizer streams. The presented values were computed by averaging the local values of mixture fraction, along  $y$ -direction in the region covering the spark, at the  $x$ - $y$  plane. As an effect of large volatility of the ethanol it can be seen that the fuel prevails even far from the spark position, however, the highest values are found only in its vicinity. In theory the higher turbulence level should increase the droplet dispersion, thus decreasing the peak values of  $\xi$  and thickening the mixing region. This is however, not the case in the current analysis and the profiles seem to be only slightly dependent on the initial

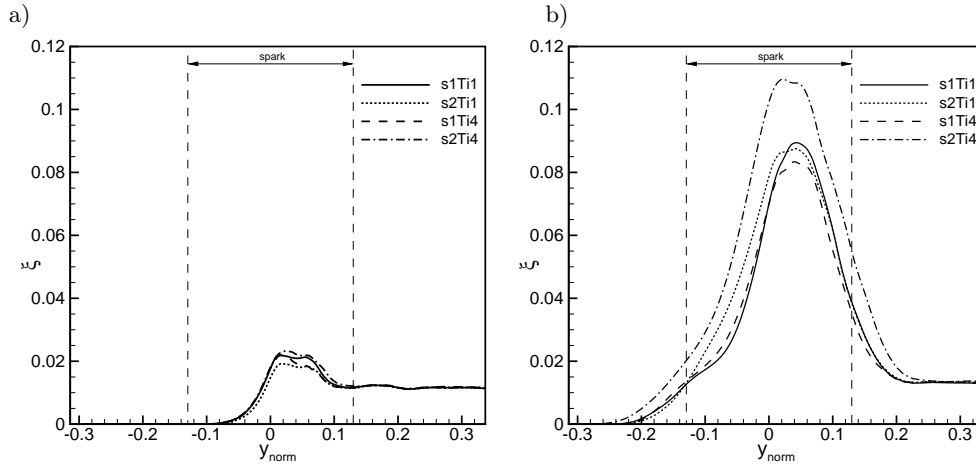


FIG. 6. Plots of the averaged mixture fraction  $\xi$  values along the  $y$ -direction in two time instances  $1.2t_{sp}$  (a) and  $1.4t_{sp}$  (b).

velocity fluctuations level. Hence, one may conclude that in the analysed cases the evaporation process is determined mainly by the thermal effects and the convective or buoyancy forces have a small impact. The maximum values of the profiles are close to the stoichiometry  $\xi_{st} = 0.1$  and as one could expect they are all tilted towards the fuel-rich side. This explains why the flame has a tendency to propagate in this direction.

### 3.2. Scatter plots

The behaviour of the flame in the mixture fraction space is analysed through the scatter plots based on the values collected in a box  $L_x \times L_z \times 14\delta$  covering the region where the flame kernel is established. Figure 7 shows distributions of the reaction rate  $\dot{\omega}$  in the range of  $\xi \in (0, 0.12)$  at two time instances, i.e.,  $1.2t_{sp}$  and  $1.4t_{sp}$ . Two distinct peaks of reaction rate are related to two different combustion regimes. The first one corresponds to the lean flame appearing in the air stream, to which fuel vapour diffuses. The second peak corresponds to the richer flame that is localized in the droplet laden stream. The results from the remaining cases vary only by different dispersion of the scatter points but qualitatively they present the same characteristics.

Scatter plots presenting the fuel mass fraction  $Y_f$  of the gaseous fuel are shown in Fig. 8. It can be seen that at the early time after the ignition ( $1.2t_{sp}$ ) the  $Y_f$  exhibits linear correlation with the mixture fraction. This is attributed to the fact that initially the flame region where the gaseous fuel is consumed is small and therefore  $Y_f$  is directly proportional to  $\xi$ . After a while the flame propagates

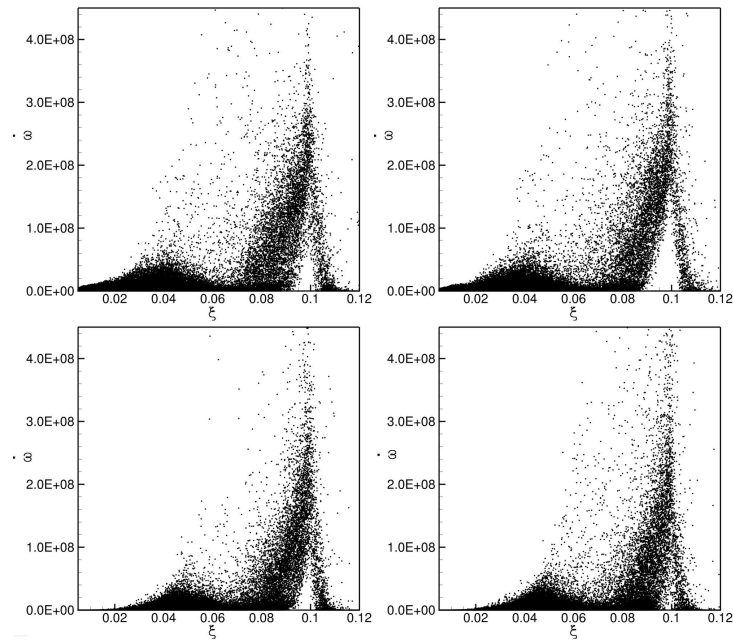


FIG. 7. Scatter plots of fuel reaction rate  $\dot{\omega}$  over the mixture fraction  $\xi$  range at  $1.2t_{sp}$  (upper figures) and  $1.4t_{sp}$ . Left column – case s1Ti1, right column – case s1Ti4.

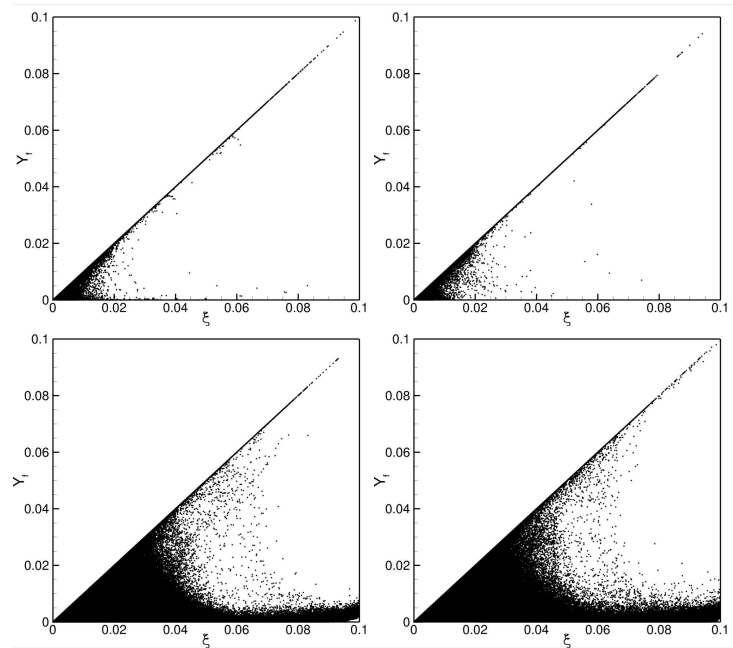


FIG. 8. Scatter plots of fuel mass fraction  $Y_f$  over the mixture fraction  $\xi$  range at  $1.2t_{sp}$  and  $1.4t_{sp}$ . Left column – case s1Ti1, right column – case s1Ti4.

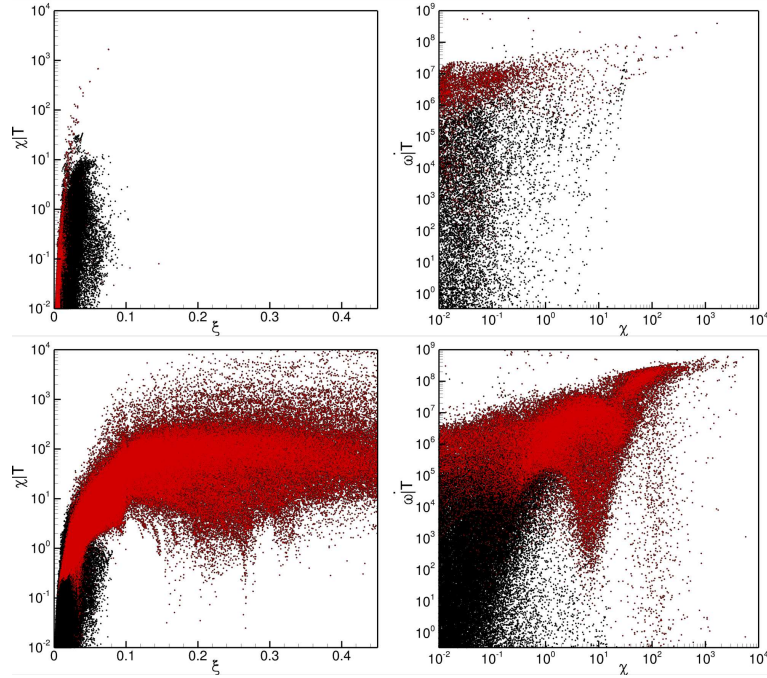


FIG. 9. Scatter plots of scalar dissipation rate  $\chi$  over the mixture fraction  $\xi$  range (left column) and reaction rate  $\dot{\omega}$  over the scalar dissipation rate  $\chi$  (right column) conditioned by high temperature value ( $T = 1000$  K red dots) in subsequent time instances ( $1.05t_{sp}$  and  $1.4t_{sp}$ ).

and combustion products arise in a larger part of the domain. The evaporation process intensifies and there are regions where the fuel, which diffuses from the droplets remains unburnt. This is manifested by visible scattering of the points at larger values of the mixture fraction.

An increase in turbulence fluctuations level increases the turbulent mixing and thus the heat transfer rate from the hot flame to the neighbouring gas and droplets. The intensity of the mixing can be characterised by the scalar dissipation rate  $\chi$  shown in Fig. 9. The red points correspond to values conditioned by the temperature  $T > 1000$  K linked with the flame's reactive layer. One can observe that during the spark duration the high temperature points occur on the lean-fuel side at very low scalar dissipation rates. In the premixed combustion mode the reaction rate and temperature increase with decreasing mixture fraction gradients, similarly as in the presented results. Later on, the scalar dissipation rate raises and eventually remains at a constant level over the wide range of mixture fraction space. The results presented in Figs. 7 and 9 show negative correlations between the  $\dot{\omega}$  and  $\chi$ , which is in good agreement with findings of CHAKRABOTRY *et al.* [14].

#### 4. Conclusions

The findings from the current studies are aligned with the two fundamental results obtained in the previous research, i.e., the spark discharge creates highly heated zone that initiates the reaction. The heated gas causes evaporation and produces a mixture within flammability limits. On the other hand, the present results are somewhat in a contradiction to the observation that for higher turbulence intensity an increased level of mixing enhances the heat diffusion into the cold regions thus precluding the reaction. The current results show a very small influence of the turbulence intensity if the flow field contains velocities with low RMS value. At the initial phase of the flame kernel propagation, no visible differences were observed for distinct turbulence intensities (i.e. 1% and 4%). Such a result is caused predominantly by two reasons: (i) strong spark energy input exceeds the minimum ignition energy and (ii) as long as RMS velocity is significantly lower than the flame speed, the ignition encounters a little influence from the flow field.

#### Acknowledgements

This work was supported by the grant 2015/17/B/ST8/03217 (National Science Centre, Poland) and statutory funds BS/PB-1-103-3010/11/P. The PL-Grid infrastructure was used to carry out the computations.

#### References

1. E. MASTORAKOS, *Ignition of turbulent non-premixed flames*, Progress in Energy and Combustion Science, **35**, 57–97, 2009.
2. J. RÉVEILLON, F.X. DEMOULIN, *Effects of the preferential segregation of droplets on evaporation and turbulent mixing*, Journal of Fluid Mechanics, **583**, 273–302, 2007.
3. A. TYLISZCZAK, E. MASTORAKOS, *LES/CMC predictions of spark ignition probability in a liquid fuelled swirl combustor*, 51st AIAA Aerospace Sciences Meeting, Paper No. AIAA 2013-0427, January 7–10, Grapevine (Dallas/Ft. Worth Region), Texas, 2013.
4. E. MASTORAKOS, *Forced ignition of turbulent spray flames*, Proceedings of the Combustion Institute, **36**, 2367–2383, 2016.
5. E. MACHOVER, E. MASTORAKOS, *Numerical investigation of the stochastic behaviour of light-round in annular non-premixed combustors*, Combustion Science and Technology, **189**, 1326–1353, 2017.
6. E. MACHOVER, E. MASTORAKOS, *Experimental investigation on spark ignition of annular premixed combustors*, Combustion and Flame, **178**, 148–157, 2017.
7. A.D. BIRCH, D.R. BROWN, M.G. DODSON, *Ignition probabilities in turbulent mixing flows*, Proceedings of the Combustion Institute, **18**, 1775–1780, 1981.

8. M.T.E. SMITH, A.D. BIRCH, D.R. BROWN, M. FAIRWEATHER, *Studies of ignition and flame propagation in turbulent jets of natural gas, propane and a gas with a high hydrogen content*, Proceedings of the Combustion Institute, **21**, 1403–1408, 1986.
9. W.P. JONES, A. TYLISZCZAK, *Large eddy simulation of spark ignition in a gas turbine combustor*, Flow, Turbulence and Combustion, **85**, 711–734, 2010.
10. A. EYSSARTIER, B. CUENOT, L.Y.M. GICQUEL, T. POINSOT, *Using LES to predict ignition sequences and ignition probability of turbulent two-phase flames*, Combustion and Flame, **160**, 1191–1207, 2013.
11. A. TYLISZCZAK, D.E. CAVALIERE, E. MASTORAKOS, *LES/CMC of blow-off in a liquid fuelled swirl burner*, Flow, Turbulence and Combustion, **292**, 237–267, 2014.
12. A. NEOPHYTOU, E. MASTORAKOS, R.S. CANT, *DNS of spark ignition and edge flame propagation in turbulent droplet-laden mixing layers*, Combustion and Flame, **157**, 1071–1086, 2010.
13. A.P. WANDEL, *Influence of scalar dissipation on flame success in turbulent sprays with spark ignition*, Combustion and Flame, **161**, 2579–2600, 2014.
14. N. CHAKRABORTY, E. MASTORAKOS, R.S. CANT, *Effects of turbulence on spark ignition in inhomogeneous mixtures: a direct numerical simulation (DNS) study*, Combustion Science and Technology, **179**, 293–317, 2007.
15. A. NEOPHYTOU, E. MASTORAKOS, R.S. CANT, *Complex chemistry simulations of spark ignition in turbulent sprays*, Proceedings of the Combustion Institute, **33**, 2135–2142, 2011.
16. N. CHAKRABORTY, E. MASTORAKOS, *Direct numerical simulations of localised forced ignition in turbulent mixing layers: The effects of mixture fraction and its gradient*, Flow, Turbulence and Combustion, **80**, 155–186, 2008.
17. S.F. AHMED, E. MASTORAKOS, *Spark ignition of lifted turbulent jet flames*, Combustion and Flame, **146**, 215–231, 2006.
18. S.F. AHMED, R. BALACHANDRAN, E. MASTORAKOS, *Measurements of ignition probability in turbulent non-premixed counterflow flames*, Proceedings of the Combustion Institute, **31**, 1507–1513, 2007.
19. S.F. AHMED, R. BALACHANDRAN, T. MARCHIONE, E. MASTORAKOS, *Spark ignition of turbulent nonpremixed bluff-body flames*, Combustion and Flame, **151**, 366–385, 2007.
20. A.W. VREMAN, *An eddy-viscosity subgrid-scale model for turbulent shear flow: Algebraic theory and applications*, Physics of Fluids, **16**, 3670–3681, 2004.
21. R.S. MILLER, K. HARSTAD, J. BELLAN, *Evaluation of equilibrium and non-equilibrium evaporation models for many-droplet gas-liquid flow simulations*, International Journal of Multiphase Flow, **24**, 1025–1055, 1998.
22. G. LACAZE, E. RICHARDSON, T. POINSOT, *Large eddy simulation of spark ignition in a turbulent methane jet*, Combustion and Flame, **156**, 1993–2009, 2009.
23. C. DUWIG, K.J. NOGENMYR, C.K. CHAN, M.J. DUNN, *Large eddy simulations of a piloted lean premix jet flame using finite-rate chemistry*, Combustion Theory and Modelling, **15**, 537–568, 2011.

- 
24. E. FERNANDEZ-TARRAZO, A.L. SÁNCHEZ, A. LIÑÁN, F.A. WILLIAMS, *A simple one-step chemistry model for partially premixed hydrocarbon combustion*, *Combustion and Flame*, **147**, 32–38, 2006.
  25. A. TYLISZCZAK, *A high-order compact difference algorithm for half-staggered grids for laminar and turbulent incompressible flows*, *Journal of Computational Physics*, **276**, 438–467, 2014.
  26. A. TYLISZCZAK, *High-order compact difference algorithm on half-staggered meshes for low Mach number flows*, *Computers and Fluids*, **127**, 131–145, 2016.
  27. A. ROSIAK, A. TYLISZCZAK, *LES-CMC simulations of a turbulent hydrogen jet in oxy-combustion regimes*, *International Journal of Hydrogen Energy*, **41**, 9705–9717, 2016.
  28. L. KUBAN, J. STEMPKA, A. WAWRZAK, A. TYLISZCZAK, *DNS and ILES study of ethanol spray forced-ignition in a time-evolving mixing layer*, Tenth Mediterranean Combustion Symposium, September 17–21, Naples, 2017.
  29. J. STEMPKA, *Impact of subgrid modelling and numerical method on autoignition simulation of two-phase flow*, *Archives of Thermodynamics*, **39**, 55–72, 2018.
  30. A. WAWRZAK, A. TYLISZCZAK, *Implicit LES study of spark parameters impact on ignition in a temporally evolving mixing layer between H<sub>2</sub>/N<sub>2</sub> mixture and air*, *International Journal of Hydrogen Energy*, **43**, 9815–9828, 2018.
  31. T. PASSOT, A. POUQUET, *Numerical simulation of compressible homogeneous flows in the turbulent regime*, *Journal of Fluid Mechanics*, **181**, 441–466, 1987.

Received July 28, 2018; revised version November 29, 2018.

---